

ARTICLE

Received 9 Sep 2014 | Accepted 26 Nov 2014 | Published 7 Jan 2015

DOI: 10.1038/ncomms6959

Large resistivity modulation in mixed-phase metallic systems

Yeonbae Lee^{1,*}, Z.Q. Liu^{2,*}, J.T. Heron³, J.D. Clarkson¹, J. Hong⁴, C. Ko¹, M.D. Biegalski², U. Aschauer⁵, S.L. Hsu¹, M.E. Nowakowski⁴, J. Wu^{1,6}, H.M. Christen², S. Salahuddin⁴, J.B. Bokor^{4,6}, N.A. Spaldin⁵, D.G. Schlom^{3,7} & R. Ramesh^{1,6,8,9}

In numerous systems, giant physical responses have been discovered when two phases coexist; for example, near a phase transition. An intermetallic FeRh system undergoes a first-order antiferromagnetic to ferromagnetic transition above room temperature and shows two-phase coexistence near the transition. Here we have investigated the effect of an electric field to FeRh/PMN-PT heterostructures and report 8% change in the electrical resistivity of FeRh films. Such a ‘giant’ electroresistance (GER) response is striking in metallic systems, in which external electric fields are screened, and thus only weakly influence the carrier concentrations and mobilities. We show that our FeRh films comprise coexisting ferromagnetic and antiferromagnetic phases with different resistivities and the origin of the GER effect is the strain-mediated change in their relative proportions. The observed behaviour is reminiscent of colossal magnetoresistance in perovskite manganites and illustrates the role of mixed-phase coexistence in achieving large changes in physical properties with low-energy external perturbation.

¹Department of Materials Science and Engineering, University of California, Berkeley, California 94720, USA. ²Oak Ridge National Laboratory, Center for Nanophase Materials Sciences, Oak Ridge, Tennessee 37831, USA. ³Department of Materials Science and Engineering, Cornell University, Ithaca, New York 14853, USA. ⁴Department of Electrical Engineering and Computer Sciences, University of California, Berkeley, California 94720, USA. ⁵Materials Theory, ETH Zurich, Wolfgang-Pauli-Strasse 27, CH-8093 Zürich, Switzerland. ⁶Materials Sciences Division, Lawrence Berkeley National Laboratory, Berkeley, California 94720, USA. ⁷Kavli Institute at Cornell for Nanoscale Science, Ithaca, New York 14853, USA. ⁸Department of Physics, University of California, Berkeley, California 94720, USA. ⁹Oak Ridge National Laboratory, Oak Ridge, Tennessee 37831, USA. * These authors contributed equally to this work. Correspondence and requests for materials should be addressed to R.R. (email: rramesh@berkeley.edu).

The past decades have witnessed dramatic discoveries in carrier-doped, strongly correlated complex oxides, typified by the emergence of high-temperature superconductivity in doped antiferromagnetic (AFM) cuprates and colossal magnetoresistance (CMR) in doped manganites^{1,2}; interestingly, reversible resistance switching induced by external electric fields on various manganites shows large electroresistance (ER) response and provides a great potential as an emerging non-volatile memory technology^{3–6}. Although the detailed mechanism of high-temperature superconductivity remains to be understood, CMR effect in the manganites is known to result from coexisting and competing ferromagnetic (FM) metallic and AFM-insulating phases in the CMR regime^{7,8}. An analogous response caused by mixed-phase coexistence in non-magnetic, uncorrelated oxides is found in the relaxor family of ferroelectrics, in which large dielectric and piezoelectric responses are observed near morphotropic phase boundaries^{9,10}. In thin-film BiFeO₃, epitaxial strain leads to the formation of a nanoscale, mixed-phase ensemble of two crystal structures that can be reversibly transformed between each other with electric fields, leading to large piezoelectric responses^{11,12}. Although these examples (as a direct consequence of mixed-phase coexistence) all occur in systems that are insulating (at least until chemically doped), we extend the same concept to metallic systems of FeRh in this report. FeRh exhibits a temperature-dependent first-order phase transition at ~ 100 °C from an AFM (low temperature) to a FM (high temperature) phase that is characterized by 1% expansion in the volume^{13–19}. Although the origin of the phase transition has long been a subject of theoretical studies^{20,21}, it is now believed to result from different temperature dependencies of the entropy in the two phases^{22,23}. The transition has recently been shown to persist in thin films^{17,24} and the substrate dependence of the transition has been exploited in heterostructures of FeRh deposited on ferroelectric BaTiO₃ to induce the FM to AFM transition using an electric field²⁵. We report large electric-field-induced changes in resistivity in a thin film of the intermetallic FeRh deposited on a piezoelectric substrate and demonstrate that the response results from the competition between coexisting AFM and FM phases with different resistivities.

Results

Growth and characterization. We deposit FeRh films onto single crystals of [001]-oriented relaxor ferroelectric 0.72PbMg_{1/3}Nb_{2/3}O₃-0.28PbTiO₃ (PMN-PT)^{26–28} using both molecular-beam epitaxy (MBE) and ultra-high vacuum sputtering techniques. Details of the synthesis protocols used in our study, and both the structural and chemical characterizations are provided in the Methods section at the end and the Supplementary Information (Supplementary Figs 1,2 and 3). Structural studies using X-ray diffraction (XRD) (Supplementary Fig. 1) show that the FeRh layer grows in a highly [001]-oriented manner on the PMN-PT [001] substrate. In the MBE-grown films (Supplementary Fig. 2), *in situ* reflection high-energy electron diffraction patterns indicate that the FeRh grew epitaxially. In the following discussion, all the measurements were performed on the films grown by sputtering, unless stated otherwise.

Magnetic force microscopy. In other previous works on FeRh systems, the temperature dependence of magnetic force microscopy (MFM), FM resonance and photoemission electron microscopy have been used to study the dynamics and nucleation of the AFM–FM phase transition^{29–32}. In this work, we use MFM to determine the temperature dependence of the magnetic state of the as-grown (or a virgin) FeRh film. Figure 1 shows MFM images obtained from the same location on the film at a series of

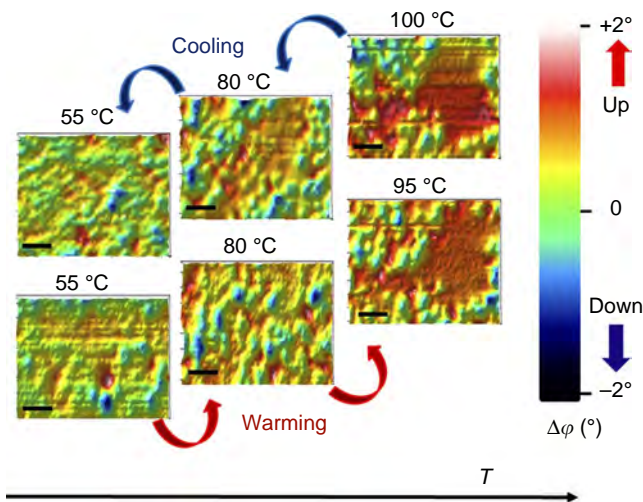


Figure 1 | MFM images of a FeRh thin film sputtered on a PMN-PT substrate. The false colour indicates the strength and orientation of the magnetic moment (red colour indicates up moment and blue colour down). At low temperature, the non-magnetic signal ($\Delta\phi \sim 0$, green colour) of the AFM state dominates and the proportion of magnetic signal from the FM phase increases with temperature. Note that even at 100 °C, which is above the phase-transition temperature, the MFM image shows a coexistence of the AFM phase with the dominant FM phase. Scale bar, 500 nm (black).

temperatures across the AFM–FM phase transition. The colours represent the relative values of phase shift $\Delta\phi$ measured via dynamic mode MFM and are proportional to the local magnetic field strength and, hence, the proportion of the FM phase. Starting at 55 °C (bottom left in Fig. 1) where the AFM phase is dominant, the sample was progressively warmed up to 100 °C, where the FM state is the dominant phase with a small fraction of the AFM phase persisting. On cooling, the fraction of FM phase progressively decreases till 55 °C, at which point the initial AFM-dominant state is restored. These changes in the MFM image and thus the magnetic states are repeatable over different regions of the sample and in multiple samples. Note that the mixed phase is disordered, with no preferred crystallographic orientations for the interfaces between the FM and AFM phases, reminiscent of the behaviour in the CMR manganites^{7,8}.

Electrical transport measurement. In the following sections, we investigate the transport behaviour. Figure 2a shows a schematic of the four-probe test structure that was used to carry out the electrical transport measurements. In Fig. 2b, we show the measured resistance R and the corresponding resistivity ρ as a function of temperature T at various electric fields E for a 50-nm-thick FeRh film, both during cooling and warming; the hysteresis is characteristic of a first-order phase transition, consistent with the magnetic property measurements (Supplementary Figs 4 and 5).

First, we discuss the zero-field ($E = 0$) case or a virgin state (Fig. 2b, red curve). Note that a virgin state is the as-grown FeRh state without any history of E -field applied on the system (no history of pre-poled state). However, regardless of any pre-poled state, the virgin state can easily be recovered by heating up the system up to 150 °C, which is above the Curie temperature (~ 140 °C) of PMN-PT used in this work, and brought back to room temperature. In this way, we observed strong reproducibility and consistency in resistivity measurement between each thermal cycle at $E = 0$ case, even after the pre-existing poled ($E \neq 0$) state. We see that the room-temperature ρ of the AFM phase is ~ 160 $\mu\Omega$ cm, which is comparable to the values in the

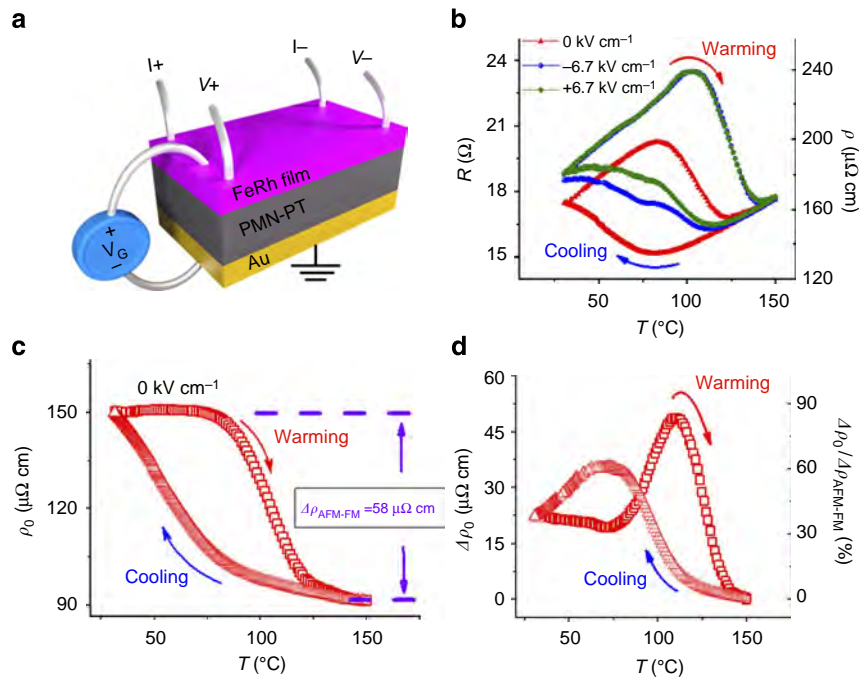


Figure 2 | Device geometry and electrical transport measurement of FeRh/PMN-PT heterostructure. (a) Schematic of the four-probe device in which the E -field is applied across the FeRh/PMN-PT/Au sandwich structure. (b) $\rho - T$ (or $R - T$) curve for E -field values of 0 (red), $+6.7 \text{ kV cm}^{-1}$ (green) and -6.7 kV cm^{-1} (blue). Hysteresis is clearly visible, with the arrows indicating the warming (red) and cooling (blue) processes. Note that the $\rho - T$ curve at $E = +6.7 \text{ kV cm}^{-1}$ and -6.7 kV cm^{-1} are indistinguishable during the warming. (c) $\rho_0 (E = 0)$ as a function of T is plotted for the zero-field case. $\Delta\rho_{\text{AFM-FM}}$ is defined to be the intrinsic resistivity difference between the AFM and FM phases under no external E -field and is equal to $58 \mu\Omega \text{ cm}$. (d) The plots of $\Delta\rho_0$ (left y axis) and $\Delta\rho_0/\Delta\rho_{\text{AFM-FM}}$ (right y axis) versus T . The warming and cooling curves show maximum values in $\Delta\rho_0/\Delta\rho_{\text{AFM-FM}}$ of $\sim 80\%$ and $\sim 63\%$ at 110°C and 75°C , respectively.

literature^{33,34}. The different intrinsic resistivities of the AFM and FM phases, namely $\Delta\rho_{\text{AFM-FM}}$, are not apparent in Fig. 2b because of the usual linear increase in metallic resistance with temperature; therefore, we show in Fig. 2c a compensated resistivity $\rho_0 (E = 0)$, which we obtained by removing the linear background increase from the raw data. The linear fitting of the form $\rho_{\text{linear}} = \alpha (T - T_0)$, where α is the temperature coefficient and T_0 is a reference temperature, was performed in the AFM state over the $30 \sim 70^\circ \text{C}$ temperature range; this fit was then subtracted from the raw data. We chose $T_0 = 30^\circ \text{C}$ so that the resistivity value after removing the linear background is the same as the raw data at $T = 30^\circ \text{C}$; this offset correction, however, is irrelevant in extracting desired $\Delta\rho_{\text{AFM-FM}}$ values. In Fig. 2c, $\Delta\rho_{\text{AFM-FM}}$ is clearly visible and is equal to around $58 \mu\Omega \text{ cm}$. This change in the resistivity is qualitatively consistent with our first-principles density functional calculations (Supplementary Fig. 6), which indicate a large difference in the carrier concentrations at the Fermi level between the FM and AFM phases.

Next we discuss the E -field dependence of the transport measurement. In Fig. 2b, we see that both positive (green line) and negative (blue line) E -fields lead to an increase in resistivity over the zero-field case at all temperatures below 140°C . As the AFM phase has a higher resistivity than the FM phase, this suggests that the E -field increases the fraction of AFM relative to FM phase. Here we attempt to quantify this fractional change between AFM and FM state driven by the E -field. First, we compare the difference in $\rho_0 (E)$ values at two fields of $E = 0$ and -6.7 kV cm^{-1} . Their differences $\Delta\rho_0 = \rho_0 (E = -6.7 \text{ kV cm}^{-1}) - \rho_0 (E = 0)$ as a function of T are shown in Fig. 2d (left y axis). Comparing this value with previously calculated $\Delta\rho_{\text{AFM-FM}}$, we obtain a ratio $\Delta\rho_0/\Delta\rho_{\text{AFM-FM}}$ as plotted in Fig. 2d (right y axis). This ratio can be interpreted as the relative fractional change of

AFM and FM states with respect to the as-grown states ($E = 0$) and is an indicator of the efficacy with which the E -field is converting the FM into the AFM phase.

Electro-magnetic coupling. For further understanding of the magnetic state change in FeRh by an applied E -field, we measured resistivity versus E -field at a fixed temperature (isothermal $\rho - E$ curve) close to the phase transition. In Fig. 3a, we show the relative change in resistivity as function of an applied E -field, defined as $\Delta\rho/\rho_{\text{min}} = [\rho(E) - \rho_{\text{min}}]/\rho_{\text{min}}$, where ρ_{min} is the minimum resistivity taken at a given isothermal $\rho - E$ curve, for various temperatures near the transition. We term this relative change the ‘giant ER’ (GER) effect. Interestingly, we find a clear hysteresis in $\Delta\rho/\rho_{\text{min}}$ versus E curves at all the temperatures presented here. In Fig. 3b, we show the maximum values of $\Delta\rho/\rho_{\text{min}}$ as a function of temperature. Note that these are unusually large for a metallic system, reaching the maximum value of $\sim 8\%$ at 95°C near the middle of the magnetic phase transition.

Discussion

To investigate the electro-magnetic coupling of the FeRh/PMN-PT heterostructure, we measured net polarization P_{net} versus E -field of the PMN-PT along the [001] out-of-plane (OOP) direction (black dashed line in Fig. 3a). Following a theory of ferroelectrics³⁵ and a ferroelectric switching model^{36,37}, a strain can be expressed as a function of P_{net} and vice versa. According to this model, OOP strain in PMN-PT reaches maximum values (tensile strain) when an absolute value of the net polarization $|P_{\text{net}}|$ takes its maximum at $E = \pm 6.7 \text{ kV cm}^{-1}$. On the other hand, the strain reaches zero state when $|P_{\text{net}}|$ becomes zero at $E = \pm 1.2 \text{ kV cm}^{-1}$; these values are coercive

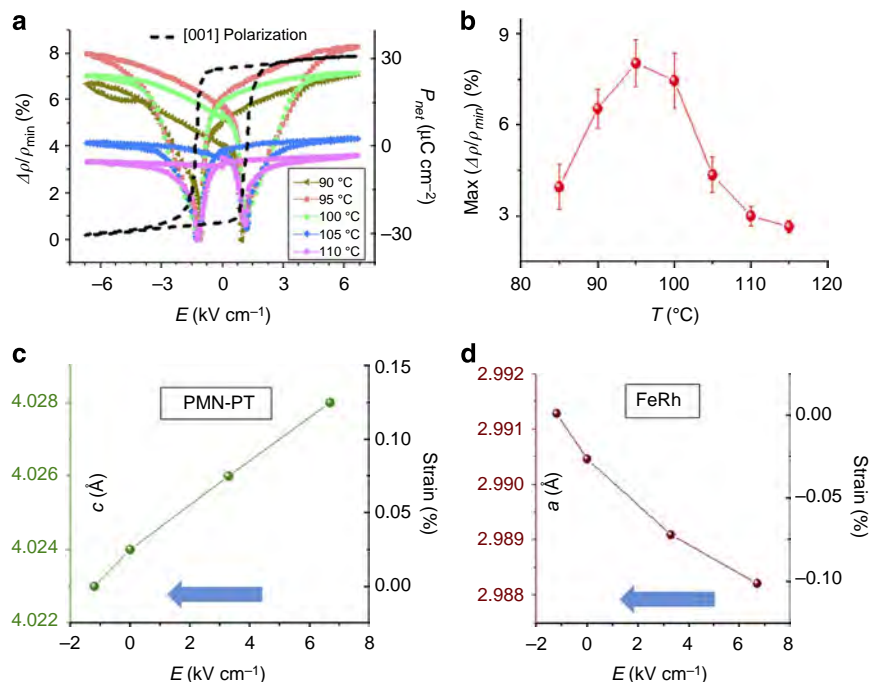


Figure 3 | The strain-mediated GER effect. (a) $\Delta\rho/\rho_{\min}$ as a function of E -field (isothermal curve) for five temperatures between 90 °C and 110 °C. The net polarization along the [001] direction versus E -field of the PMN-PT substrate is overlaid (black-dashed line, right y axis). Note the coercivity E -field in the polarization curve is $\pm 1.2 \text{ kV } ^\circ\text{C cm}^{-1}$. (b) Temperature dependence of the maximum of the ratio $\Delta\rho/\rho_{\min}$, $\text{Max}(\Delta\rho/\rho_{\min})$, showing a peak value around 95 °C. To check the reproducibility of GER effect $\Delta\rho/\rho_{\min}$ versus E curves were measured repeatedly during a thermal cycling of warming up to 150 °C, cooling down to room temperature, then brought back to the same temperatures where the curves were taken. Remarkably, the data show strong reproducibility during these thermal cycling processes and the error bar in the graph was estimated to account for the small variations in $\text{Max}(\Delta\rho/\rho_{\min})$ between the cycles. Lower panels are the lattice constant change (left y axes) and the strain (right y axes) of PMN-PT (c) and FeRh (d) along their crystalline axes, obtained from XRD measurements with *in situ* E -field application. The maximum compressive IP strain induced in FeRh is 0.1% at E -field of $+6.7 \text{ kV cm}^{-1}$. The blue arrows indicate the measurement direction.

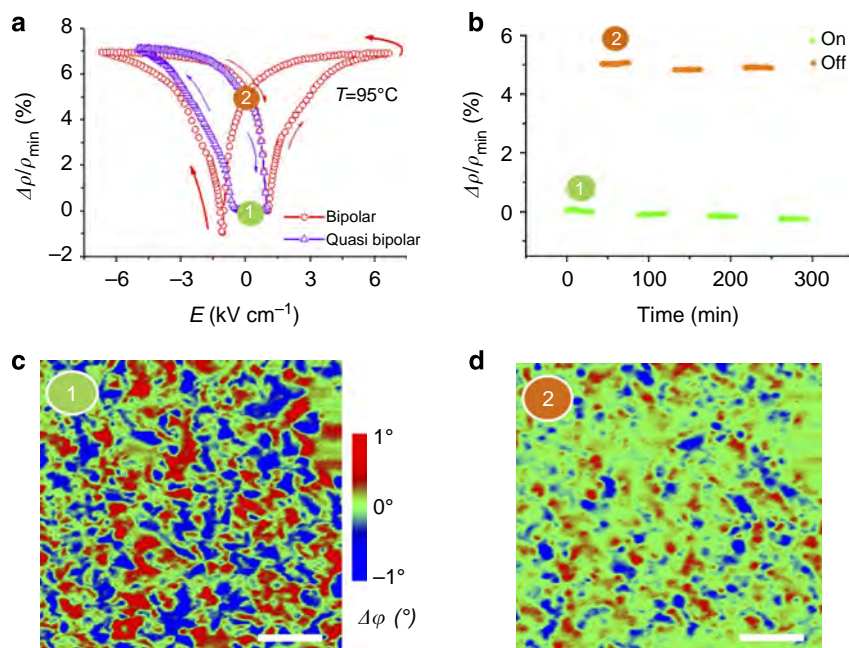


Figure 4 | Potential application to ferroelectric RAM memory device and magnetic phase modulation by electric field. (a) $\Delta\rho/\rho_{\min}$ versus E -field in bipolar and quasi-bipolar curves. Continuous DC E -fields were used in the plot and the arrows indicate the direction of the E -field sweep. (b) The plot shows $\Delta\rho/\rho_{\min}$ as a function of time in the 'On' state (lower ρ state, 1) and 'Off' state (higher ρ state, 2). Two different logic states were written by pulsed E -fields with the amplitudes of $+1.2 \text{ kV cm}^{-1}$ (On state, 1) and -6.7 kV cm^{-1} (Off state, 2) consecutively for each state. Each state lasts for 30 min and the On/Off states were stable and reproducible over seven consecutive sequences. Two MFM images were taken at these two states with On-state (c) and Off-state (d) reproduced by the same pulsed E -fields. The vertical colour scale bar (in the middle) shows the phase shift $\Delta\phi$ in MFM and proportional to the local magnetic moment strength. Scale bar, 1 μm (white).

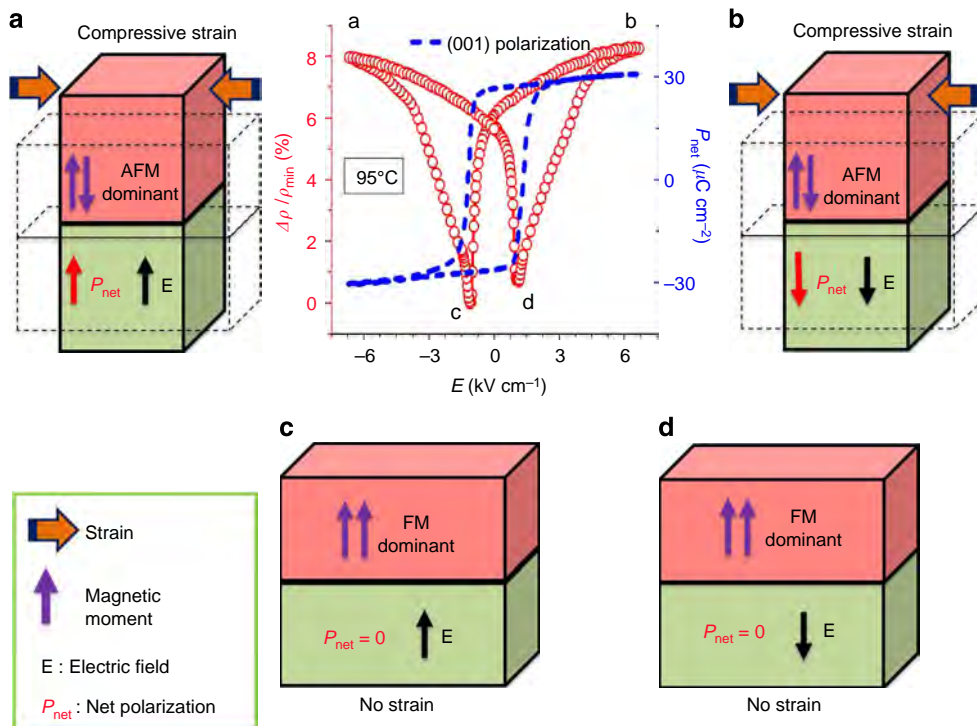


Figure 5 | Schematics for the reversible resistivity modulation by an E -field in a FeRh/PMN-PT heterostructure. (a,b) The compressive IP strain state promotes the AFM-dominant state leading to a higher resistivity state with a $\Delta\rho/\rho_{\min}$ value up to 8%. **(c,d)** No-strain state, which promotes an FM-dominant state of FeRh, and $\Delta\rho/\rho_{\min}$ takes its minimum value. The inset in the middle are plots of $\Delta\rho/\rho_{\min}$ (red, left y axis) and P_{net} (blue, right y axis) as a function of E -field.

fields of the PMN-PT polarization curve as shown in Fig. 3a. This further implies that PMN-PT is at its maximum compressive in-plane (IP) strain state at $E = \pm 6.7 \text{ kV cm}^{-1}$ and zero strain state at $E = \pm 1.2 \text{ kV cm}^{-1}$. We observed that the minimum resistivity state of the FeRh film occurs at $P_{\text{net}} = 0$, and the maximum resistivity changes occurs at the maximum value of $|P_{\text{net}}|$. Although an induced strain in a ferroelectric results from its net polarization change, the re-alignment of individual ferroelectric domains could also give rise to similar polarization change without inducing significant strain in the material. To rule out the domain re-alignment scenario and therefore validate the direct link between $|P_{\text{net}}|$ and strain induced in PMN-PT, we measured PMN-PT lattice constant changes directly using XRD with *in-situ* E -field application (please note that a larger size of FeRh/PMN-PT sample with the identical growth condition was used for XRD measurement to improve XRD diffraction intensity). The results are shown in Fig. 3c (for the complete XRD spectra, refer to Supplementary Fig. 7). Interestingly, PMN-PT shows the maximum OOP lattice constant $c = 4.028 \text{ \AA}$ at $E = + 6.7 \text{ kV cm}^{-1}$ and then monotonically decreases to the minimum value of $c = 4.023 \text{ \AA}$ as the field is brought down to -1.2 kV cm^{-1} . The direct measurement of PMN-PT c -values under E -field strongly supports that the polarization switching of PMN-PT does indeed induce the strain modulation rather than re-alignment of small domains within. We further investigated the IP lattice constant a of FeRh as function of E -field and the values are plotted in Fig. 3d. The change in a of FeRh is clearly seen and strongly correlated with the change in PMN-PT c -values. The corresponding strain modulations for both PMN-PT and FeRh are plotted in Fig. 3c,d on the right y axes. Please note that the strains are calculated with respect to the value at $E = -1.2 \text{ kV cm}^{-1}$, where $P_{\text{net}} = 0$. In other ferroelectric experiments^{26,38}, strains are usually calculated with respect to zero E -field value, to account for the pre-poled state of the

ferroelectric systems under the study. However, the choice of zero strain state in our work, to be consistent with a theory, does not alter the qualitative conclusion between the strain and resistivity changes of FeRh. With comprehensive observation of the lattice changes on both PMN-PT and FeRh, the net polarization measurement and the hysteresis behaviour in the FeRh/PMN-PT system, we conclude the induced strain to the FeRh/PMN-PT heterostructure by external E -field is responsible for the resistivity modulation of FeRh, presumably altering its magnetic property.

Lastly, we demonstrate a rudimentary manifestation of the applicability of such an approach for a potentially low-energy information storage element. In Fig. 4a, we show the hysteresis in $\Delta\rho/\rho_{\min}$ versus E -field when tested in both bipolar and quasi-bipolar cycling with continuous DC electric field. Then non-volatile logic states were written by applying pulsed-electric field with width of 1 s and amplitude of $+1.2 \text{ kV cm}^{-1}$ for the 'On' state and -6.7 kV cm^{-1} for the 'Off' state consecutively, as seen in Fig. 4b. The two logic states show strong stability and reproducibility (over the total measurement time of 5 h) and maintain clearly differentiated resistivity values in each state.

To understand the origin of resistivity modulation by E -field, two MFM images of FeRh were taken at the 'On' (Fig. 4c) and 'Off' states (Fig. 4d). The images show magnetic phase changes between these two logic states, with 'On' state (lower resistivity) showing stronger magnetic signal and the 'Off' state (higher resistivity) showing suppressed magnetic signal. The phase shift $\Delta\phi$ indicates the strength of local magnetic moments, and therefore green colours correspond to zero (or very weak) magnetic moment in the region. In both images, we observed a mixture of AFM (green) and FM (blue and red), and the difference in these two images shows that the role of the strain induce by E -field is to convert the relative ratio between them. Our first-principles density functional calculations (Supplementary Fig. 6) indicate negligible changes in the

electronic and magnetic structure of either the FM or AFM phase at the limit of two extreme cases: 0.1% tensile and compressive strain. The calculation suggests that the role of the strain is to convert between the FM and AFM phases, resulting in the large change in the resistivity observed in this experiment. Combined with the MFM observation and the density functional theory calculation, the resistivity modulation of FeRh is a direct consequence of the magnetic phase variation (or the AFM to FM ratio changes), mediated via strain modulation of ferroelectric substrate, influenced by external E -field.

In summary, we have reported the GER effect in FeRh/PMN-PT heterostructures, via the strain control of a ferroelectric substrate. Figure 5 summarizes the schematic diagram of the strain dynamics on the FeRh/PMN-PT system whose resistivity can reversibly be controlled by an external E -field. Comprehensive studies of MFM and X-ray diffractometer combined with resistivity measurements reveal that the compressive IP strain on FeRh drives the system into more AFM-dominated state, and therefore a higher resistivity state is achieved (Fig. 5a,b). On the other hand, when the system relaxes back to no-strain state, FM state is preferred (Fig. 5c,d), leading to a lower resistivity state. We showed that the origin of the resistivity change is the conversion between the coexisting FM and AFM phases of FeRh, which have different volumes and conductivities accompanying the different magnetic orderings. The strain-mediated resistivity change is large for a metallic/ferroelectric heterostructure system at E -fields of the order of $4 \sim 6 \text{ kV cm}^{-1}$, rendering the behaviour potentially technologically relevant. This sensitivity is a consequence of the fact that the FM and AFM phases are relatively close in energy near the transition temperature²⁴ and thus can be interconverted from one to the other by simply straining the lattice parameter of the system. Artificially engineered heterostructures such as spin valves or tunnel junction devices may enhance the control of resistance modulation and therefore make the GER effect found in this work more attractive for applications.

Methods

Film growth and characterization. FeRh films were fabricated by both DC sputtering and MBE techniques. For the sputtering deposition, (001)-oriented PMN-PT substrates (1- μm -thick Au layer was coated on the back side as bottom electrodes as in Fig. 2a) were heated up to 375 °C at the rate of 20 °C min⁻¹ in a base pressure of 10^{-8} Torr. Subsequently, a small amount of Ar gas was introduced into the chamber, maintaining the total pressure of 3.0 mTorr. The FeRh films were then grown from a stoichiometric Fe_{0.5}Rh_{0.5} target. After the deposition, films were heated up to 500 °C at 10 °C min⁻¹ in vacuum and annealed for 1 h and subsequently cooled to room temperature at 10 °C min⁻¹. The deposition rate was 1.75 nm min⁻¹, determined by X-ray reflectivity measurements.

MBE films were grown in a Veeco Gen10 MBE chamber with a chamber background pressure of $\sim 8 \times 10^{-9}$ Torr. The FeRh films were deposited at a substrate temperature of 420 °C. The orientation and phase purity of the growth of the epitaxial FeRh films was monitored *in situ* via reflection high-energy electron diffraction. Following the deposition, the films were annealed at the same temperature for 30 min.

XRD spectra with *in situ* E -fields were collected in a PANalytical X'Pert PRO diffractometer combined with a Keithley 2410 voltage source meter.

Chemical analysis. The chemical composition of the FeRh films was analysed by nano-Auger Electron Spectroscopy conducted in ultra-high vacuum (base pressure $\sim 10^{-10}$ mbar) using a field-emission electron source whose spot size was focused below a diameter of 10 nm and a multi-channel hemispherical energy analyser. After removal of the surface oxide layer by gentle Ar ion milling, the chemical stoichiometry of FeRh films was estimated to be Fe_{0.44}Rh_{0.56}, using primary Rh MNN and Fe LMM Auger peaks. This value is within the composition range of the FeRh α' -phase showing the AFM-FM transition.

Magnetic force microscopy. MFM measurements were acquired using a non-contact tapping mode and a dynamic lift variation with a lift height of 30 nm. This was repeated at various temperatures using a Veeco Nanoscope with the temperature control capability up to 150 °C.

Electrical transport measurement. Resistance measurements from 30 to 150 °C were carried out in a typical four-probe stage setup using the van der Pauw geometry with an external current source (Keithley-6220) and voltage meter (Keithley-2182). DC electric fields of up to $\pm 6.7 \text{ kV cm}^{-1}$ were provided by a Keithley-6517B voltage source and were applied between the top FeRh film and the bottom Au electrode on the underside of the PMN-PT substrate with the bottom electrode grounded (Fig. 2a). For the pulsed electric field used for generating the two logic states in Fig. 4b, a wave-form generator (Agilent 33250A) with a voltage amplifier was used.

Magnetic property measurements. Magnetization measurements were carried out in a superconducting quantum interference device magnetometer by Quantum Design with a maximum temperature capability of 400 K.

Density functional theory calculations. We computed the electronic densities of states of the AFM and FM phase of FeRh in the CsCl structure for two extreme cases: 0.1% tensile and compressive strain along the [100] IP direction, using Vienna *ab initio* simulation package^{39–42} with the Perdew–Burke–Ernzerhof exchange correlation functional⁴³, and projector augmented wave potentials^{44,45} with Fe (4s, 3d, 3p) and Rh (5s, 4d, 4p) valence electrons. The plane-wave cutoff was 550 eV and reciprocal space was sampled with $19 \times 19 \times 19$ and $11 \times 11 \times 11$ Γ -centred meshes for the FM and AFM ($2 \times 2 \times 2$ supercell) phases, respectively.

References

- Bednorz, J. G. & Müller, K. A. Possible high T_c superconductivity in the Ba-La-Cu-O system. *Z. Phys. B Condens. Matter* **64**, 189–193 (1986).
- Jin, S. *et al.* Thousandfold change in resistivity in magnetoresistive La-Ca-Mn-O films. *Science* **264**, 413–415 (1994).
- Odagawa, A. *et al.* Colossal electroresistance of a Pr_{0.7}Ca_{0.3}MnO₃ thin film at room temperature. *Phys. Rev. B* **70**, 224403 (2004).
- Tokunaga, Y. *et al.* Colossal electroresistance effect at metal electrode/La_{1-x}Sr_{1+x}MnO₄ interfaces. *Appl. Phys. Lett.* **88**, 223507 (2006).
- Wu, T. *et al.* Electroresistance and electronic phase separation in mixed-valent manganites. *Phys. Rev. Lett.* **86**, 5998–6001 (2001).
- Liu, S. Q., Wu, N. J. & Ignatiev, A. Electric-pulse-induced reversible resistance change effect in magnetoresistive films. *Appl. Phys. Lett.* **76**, 2749 (2000).
- Uehara, M., Mori, S., Chen, C. H. & Cheong, S.-W. Percolative phase separation underlies colossal magnetoresistance in mixed-valent manganites. *Nature* **399**, 560–563 (1999).
- Murakami, Y., Yoo, J. H., Shindo, D., Atou, T. & Kikuchi, M. Magnetization distribution in the mixed-phase state of hole-doped manganites. *Nature* **423**, 965–968 (2003).
- Newnham, R. E. Molecular mechanisms in smart materials. *MRS Bull.* **22**, 20–34 (1997).
- Ahart, M. *et al.* Origin of morphotropic phase boundaries in ferroelectrics. *Nature* **451**, 545–548 (2008).
- Zeches, R. J. *et al.* A strain-driven morphotropic phase boundary in BiFeO₃. *Science* **326**, 977–980 (2009).
- Zhang, J. X. *et al.* Large field-induced strains in a lead-free piezoelectric material. *Nat. Nanotechnol.* **6**, 98–102 (2011).
- Gruner, M., Hoffmann, E. & Entel, P. Instability of the rhodium magnetic moment as the origin of the metamagnetic phase transition in α -FeRh. *Phys. Rev. B* **67**, 064415 (2003).
- Marti, X. *et al.* Room-temperature antiferromagnetic memory resistor. *Nat. Mater.* **13**, 367–374 (2014).
- Moruzzi, V. L. & Marcus, P. M. Antiferromagnetic-ferromagnetic transition in FeRh. *Phys. Rev. B* **46**, 2864–2873 (1992).
- Stamm, C. *et al.* Antiferromagnetic-ferromagnetic phase transition in FeRh probed by x-ray magnetic circular dichroism. *Phys. Rev. B* **77**, 184401 (2008).
- Suzuki, I., Naito, T., Itoh, M., Sato, T. & Taniyama, T. Clear correspondence between magnetoresistance and magnetization of epitaxially grown ordered FeRh thin films. *J. Appl. Phys.* **109**, 07C717 (2011).
- Zsoldos, L. Lattice parameter change of FeRh alloys due to antiferromagnetic-ferromagnetic transformation. *Phys. Stat. Sol.* **20**, K25–K28 (1967).
- Swartzendruber, L. J. The Fe-Rh (Iron-Rhodium) System. *Bull. Alloy Phase Diagrams* **5**, 456–462 (1984).
- Kittel, C. Model of exchange-inversion magnetization. *Phys. Rev.* **120**, 335–342 (1960).
- Jarrett, H. S. Mechanism of the ferrimagnetic to antiferromagnetic transition in MnCrSb. *Phys. Rev.* **134**, A942–A950 (1964).
- Annaorazov, M. P., Nikitin, S., Tyurin, A., Asatryan, K. & Dvletov, A. Anomalous high entropy change in FeRh alloy. *J. Appl. Phys.* **79**, 1689–1695 (1996).
- Gu, R. & Antropov, V. Dominance of the spin-wave contribution to the magnetic phase transition in FeRh. *Phys. Rev. B* **72**, 012403 (2005).

24. Maat, S., Thiele, J.-U. & Fullerton, E. E. Temperature and field hysteresis of the antiferromagnetic-to-ferromagnetic phase transition in epitaxial FeRh films. *Phys. Rev. B* **72**, 214432 (2005).
25. Cherifi, R. O. *et al.* Electric-field control of magnetic order above room temperature. *Nat. Mater.* **13**, 345–351 (2014).
26. Thiele, C., Dörr, K., Bilani, O., Rödel, J. & Schultz, L. Influence of strain on the magnetization and magnetoelectric effect in $\text{La}_{0.7}\text{A}_{0.3}\text{MnO}_3$ / PMN-PT(001) (A = Sr,Ca). *Phys. Rev. B* **75**, 054408 (2007).
27. Biegalski, M. D., Dörr, K., Kim, D. H. & Christen, H. M. Applying uniform reversible strain to epitaxial oxide films. *Appl. Phys. Lett.* **96**, 151905 (2010).
28. Yang, L. *et al.* Bipolar loop-like non-volatile strain in the (001)-oriented $\text{Pb}(\text{Mg}_{1/3}\text{Nb}_{2/3})\text{O}_3$ - PbTiO_3 single crystals. *Sci. Rep.* **4**, 4591 (2014).
29. Mariager, S. O. *et al.* Imaging the antiferromagnetic to ferromagnetic first order phase transition of FeRh. Preprint at <http://arxiv.org/abs/1301.4164> (2013).
30. Mancini, E. *et al.* Magnetic phase transition in iron–rhodium thin films probed by ferromagnetic resonance. *J. Phys. D Appl. Phys.* **46**, 245302 (2013).
31. Yokoyama, Y. *et al.* MFM observation of magnetic phase transitions in ordered FeRh systems. *J. Magn. Magn. Mater.* **177–181**, 181–182 (1998).
32. Baldasseroni, C. *et al.* Temperature-driven nucleation of ferromagnetic domains in FeRh thin films. *Appl. Phys. Lett.* **100**, 262401 (2012).
33. De Vries, M. A. *et al.* Hall-effect characterization of the metamagnetic transition in FeRh. *New J. Phys.* **15**, 013008 (2013).
34. Van Driel, J., Coehoorn, R., Strijkers, G. J., Brück, E. & de Boer, F. R. Compositional dependence of the giant magnetoresistance in $\text{Fe}_x\text{Rh}_{1-x}$ thin films. *J. Appl. Phys.* **85**, 1026–1036 (1999).
35. Rabe, K. M., Ahn, C. H. & Triscone, J.-M. *Physics of ferroelectrics: a modern perspective* (Springer, 2007).
36. Hwang, S., Lynch, C. & McMeeking, R. Ferroelectric/ferroelastic interactions and a polarization switching model. *Acta Met. Mater.* **43**, 2073–2084 (1995).
37. Ball, B. L., Smith, R. C., Kim, S.-J. & Seelecke, S. *Smart Struct. Mater. 2005 Model. Signal Process. Control. Proc. SPIE* Vol. 5757 (2005).
38. Park, S.-E. & Shrout, T. R. Ultrahigh strain and piezoelectric behavior in relaxor based ferroelectric single crystals. *J. Appl. Phys.* **82**, 1804–1811 (1997).
39. Kresse, G. & Hafner, J. *Ab initio* molecular dynamics for liquid metals. *Phys. Rev. B* **47**, 558–561 (1993).
40. Kresse, G., Hafner, J. & Hafner, J. *Ab initio* molecular-dynamics simulation of the liquid-metal-amorphous-semiconductor transition in germanium. *Phys. Rev. B* **49**, 14251–14269 (1994).
41. Kresse, G. & Furthmüller, J. Efficiency of *ab-initio* total energy calculations for metals and semiconductors using a plane-wave basis set. *Comput. Mater. Sci.* **6**, 15–50 (1996).
42. Kresse, G. & Furthmüller, J. Efficient iterative schemes for *ab initio* total-energy calculations using a plane-wave basis set. *Phys. Rev. B* **54**, 11169–11186 (1996).
43. Perdew, J., Burke, K. & Ernzerhof, M. Generalized gradient approximation made simple. *Phys. Rev. Lett.* **77**, 3865–3868 (1996).
44. Kresse, G. & Joubert, D. From ultrasoft pseudopotentials to the projector augmented-wave method. *Phys. Rev.* **59**, 1758–1775 (1999).
45. Blochl, P. E. Projector augmented-wave method. *Phys. Rev. B* **50**, 17953–17979 (1994).

Acknowledgements

We acknowledge the support from the DARPA FENA-FAME and the NSF (Nanosystems Engineering Research Center for Translational Applications of Nanoscale Multiferroic Systems, Cooperative Agreement Award EEC-1160504). Work at Cornell University was supported in part by NSF MRSEC (DMR-1120296) through the Cornell Center for Materials Research. Work at the Oak Ridge National Laboratory (ORNL) was sponsored by the Laboratory Directed Research and Development Program of ORNL managed by UT-Battelle, LLC, for the U.S. Department of Energy, and performed at the Center for Nanophase Materials Sciences, which is sponsored at ORNL by the Scientific User Facilities Division, Office of Basic Energy Sciences, U.S. Department of Energy. We thank the support from DOD-ARO MURI, E3S and DARPA programmes. We are grateful to Dr. X. Renshaw Wang in MIT for the device schematic and Dr. D. Frank Ogletree for assisting with the nano-Auger analysis at the Molecular Foundry, which was supported by DOE under Contract No. DE-AC02-05CH11231.

Author contributions

Sample preparation, the measurement and the data analysis by Y.L., Z.L., J.T.H. and J.D.C.; MFM, nano-Auger and the structural characterization by J.H., M.D.B., S.L.H., C.K. and M.E.N.; theoretical density functional theory calculations by U.A. and N.A.S.; project initiation, guidance and supervision by M.D.B., J.W., H.M.C., S.S., J.B.B., D.G.S. and R.R.; comprehensive organization of the project by R.R.

Additional information

Supplementary Information accompanies this paper at <http://www.nature.com/naturecommunications>

Competing financial interests: The authors declare no competing financial interests.

Reprints and permission information is available online at <http://npg.nature.com/reprintsandpermissions/>

How to cite this article: Lee, Y. *et al.* Large resistivity modulation in mixed-phase metallic systems. *Nat. Commun.* 6:5959 doi: 10.1038/ncomms6959 (2015).